Cytometry
PART A
Journal of the International Society for Advancement of Cytometry

Polarization Imaging and Classification of Jurkat T and Ramos B Cells Using a Flow Cytometer

Yuanming Feng,[1] Ning Zhang,[1] Kenneth M. Jacobs,[2] Wenhuan Jiang,[2] Li V. Yang,[3,4] Zhigang Li,[3] Jun Zhang,[1] Jun Q. Lu,[2] Xin-Hua Hu[1,2]*

[1]Department of Biomedical Engineering, Tianjin University, Tianjin 300072, China

[2]Department of Physics, East Carolina University, Greenville, North Carolina 27858

[3]Department of Oncology, Brody School of Medicine, East Carolina University, Greenville, North Carolina 27834

[4]Department of Internal Medicine, Brody School of Medicine, East Carolina University, Greenville, North Carolina 27834

Received 27 December 2013; Revised 21 March 2014; Accepted 18 June 2014

Grant sponsor: North Carolina Biotechnology Center, Grant number: 2010-TEG-1501

Grant sponsor: National Science Foundation of China, Grant numbers: 81041107 and 81171342

Grant sponsor: Brody Brothers Endowment Fund, Golfers Against Cancer

Grant sponsor: The American Heart Association.

*Correspondence to: Xin-Hua Hu; Department of Biomedical Engineering, Tianjin University, Tianjin 300072, China. E-mail: hux@ecu.edu

DOI: 10.1002/cyto.a.22504

• Abstract

Label-free and rapid classification of cells can have awide range of applications in biology. We report a robust method of polarization diffraction imaging flow cytometry (p-DIFC) for achieving this goal. Coherently scattered light signals are acquired from single cells excited by a polarized laser beam in the form of two cross-polarized diffraction images. Image texture and intensity parameters are extracted with a gray level co-occurrence matrix (GLCM) algorithm to obtain an optimized set of feature parameters as the morphological "fingerprints" for automated cell classification. We selected the Jurkat T cells and Ramos B cells to test the p-DIFC method's capacity for cell classification. After detailed statistical analysis, we found that the optimized feature vectors yield accuracies of classification between the Jurkat and Ramos ranging from 97.8% to 100% among different cell data sets. Confocal imaging and three-dimensional reconstruction were applied to gain insights on the ability of p-DIFC method for classifying the two cell lines of highly similar morphology. Based on these results we conclude that the p-DIFC method has the capacity to discriminate cells of high similarity in their morphology with "fingerprints" features extracted from the diffraction images, which may be attributed to subtle but statistically significant differences in the nucleus-to-cell volume ratio in the case of Jurkat and Ramos cells.

• Key terms

flow cytometry; polarization imaging; cell classification; light scattering

Biological cells scatter light elastically due to heterogeneity in refractive index and present intriguing patterns of scattering in space. The intensity and polarization of the coherently scattered light correlate strongly with the intracellular distribution of refractive index, thus yielding the possibility for three-dimensional (3D) morphology based analysis and phenotyping of cells with no need for fluorescent or absorptive staining (1–7). Label-free cell analysis according to morphology is particularly useful for investigating cells that typically require multiple fluorescent probes or labels. Examples include classification of lymphocyte subtypes for immunotherapy of cancers (8,9), detection of circulating tumor epithelial cells in blood (10), and study of stem cells (11). Furthermore, apoptotic cells, dividing cells, and immature cells all present or undergo significant and characteristic changes in their cytoplasmic and nuclear structures and investigations of these cells proceed best with no or minimal extrageneous interferences such as staining (12,13). In these cases, rapid and morphology based classification of cells without staining can be especially beneficial and may find wide applications in basic cell biology research and drug development.

Light scattering by cells has been pursued within the platform of flow cytometry in search for accurate methods to analyze single cells by recording the scattering

ISAC
International Society for Advancement of Cytometry

patterns with discrete (2,14–16) or imaging sensors (17–23). While these studies have confirmed clearly the correlation between the intensity distribution of the scattered light and cell morphology, very little is known on how to extract quantitative feature parameters from polarized light scattering patterns for rapid and detailed analysis of cellular morphology with a flow device. Existing flow cytometric (FCM) systems acquire both fluorescent and scatter signals for cell assay. The signals from the channels of forward scatter (FSC) and side scatter (SSC), however, reflect only the cell volume and degree of heterogeneity in intracellular distribution of refractive index, which yield very limited information on cell morphology and ability to distinguish cell types or quantify morphological changes (24). It has been shown that even with angle-resolved measurement of scattered light one cannot distinguish the T and B lymphocytes (25). Previously we have developed a jet-in-fluid design of flow chamber and an objective based off-focus imaging scheme to acquire high-contrast diffraction images from cells carried by the core fluid of a laminar flow (19,20,23,26). Unpolarized images were acquired with one CCD camera and automated image analysis software codes based on Fourier, Gabor transfer, and gray level co-occurrence matrix (GLCM) algorithm were developed to rapidly extract image feature parameters (22,23,27). The above approach has been termed as the diffraction imaging flow cytometry (DIFC) method to stress the coherent nature of the methodology that otherwise would be impossible using an incoherent light source such as xenon lamp for cell excitation.

We have recently improved the DIFC method by simultaneously acquiring two cross-polarized diffraction images or a polarization image pair per cell and developed an image processing and statistical analysis software to take the full advantage of the image pair data for cell classification. The improvement leads to the polarization DIFC (p-DIFC) method, which enables for the first time extraction of information from polarized light scattering patterns for detailed and label-free analysis of cells in an imaging flow cytometer. In this report, we present the results of flow cytometric measurement and statistical analysis of cross-polarized diffraction image pairs acquired from the Jurkat T and Ramos B cells, which were derived from malignant human lymphocytes. Light scatter and fluorescence signals were also measured from unstained and CD marker stained Jurkat and Ramos cells using a conventional flow cytometer to compare with the p-DIFC data. Furthermore, we performed confocal imaging on the two cell lines to quantitatively compare their 3D morphology and gain insights on the capability of the p-DIFC method for distinction of the two cell lines.

MATERIALS AND METHODS

Cell Preparation and Conventional Flow Cytometric Measurement

Jurkat and Ramos cells (ATCC, Manassas, VA), derived, respectively, from human acute leukemia T and Burkitt lymphoma B lymphocytes, were cultured in the RPMI 1640 medium supplemented with 10% fetal bovine serum (Life Technologies, Carlsbad, CA). Both cell lines were grown under the same condition in a humidified tissue culture incubator filled with 5% CO_2 at 37°C. Viability of the cells for the p-DIFC measurements was checked by the trypan blue exclusion test and percentages of viable cells were found to be approximately 98%. A conventional flow cytometer (FACScan, Becton Dickinson) was used to measure the forward and side light scatter of the unstained cells. Both light scatter and fluorescence signals were acquired from the cell lines co-stained with the anti-human T cell marker CD3 (CD0304, Life Technologies) and the B cell marker CD19 (MHCD1901, Life Technologies).

The p-DIFC Measurement

Details on the fluidic design of the p-DIFC method have been given elsewhere (19,20,26). Briefly a “jet-in-fluid” flow chamber design and an off-focus imaging configuration have been developed and improved to markedly reduce the diffraction image noise (19,20) by eliminating refractive index-mismatched interfaces near the imaged cells. A syringe pump was used to drive the cell suspension in the RPMI 1640 media as the core fluid into the flow chamber through a round glass tube of inside diameter of 200 μm. With a concentric sheath fluid at a higher pressure entering the same chamber, the cells carried by the hydrodynamically focused core fluid move in single-file and each elastically scatters light as it passes through the focus of an incident beam. A continuous-wave solid state laser (DPSS-532, Coherent) was used to produce the incident beam of 532 nm in wavelength, 100 mW in power, and TEM_{00} beam profile which was linearly polarized with its direction set at horizontal, vertical or 45° from horizontal using a half-wave plate. The side scatter signals were collected with an infinity-corrected 50× objective of $NA = 0.55$ (378–805-3, Mitutoyo) followed by an interference filter of transmission band centered at 532 nm with a bandwidth of 10 nm (FL532-10, Thorlabs) and a polarizing beam splitter (PBS251, Thorlabs). This allows acquisition of two cross-polarized diffraction images per cell. The pair consists of s- and p-polarized images to record scattered light of vertical and horizontal polarization, respectively. The two CCD cameras (LU075M, Lumenera) used to acquire and output the data with images of 640 × 480 pixels and 12-bit pixel depth. A schematic of the p-DIFC system is shown in Figure 1.

The polarizing split-view imaging unit consisting of the objective, optics, and cameras was first aligned under a white light incoherent illumination to focus on the cross point of the hydrodynamically focused core fluid with incident beam focus. Afterward, the imaging unit was translated toward the flow chamber by a distance of $\Delta x = 100\ \mu m$ for diffraction imaging of the cells with the white light turned off. The speed of image acquisition varies from 1 to 5 frame/s with the cameras’ exposure time set at 1 ms and cells flowing at a very low speed of about 4 mm/s through the incident laser beam to reduce blurring (26). Each cell suspension was diluted to a concentration of about 10^5 cells/ml and injected into the core reservoir at room temperature of 22°C. The power of the incident laser beam was adjusted from 8 to 74 mW with neutral density filters when the incident beam’s polarization was

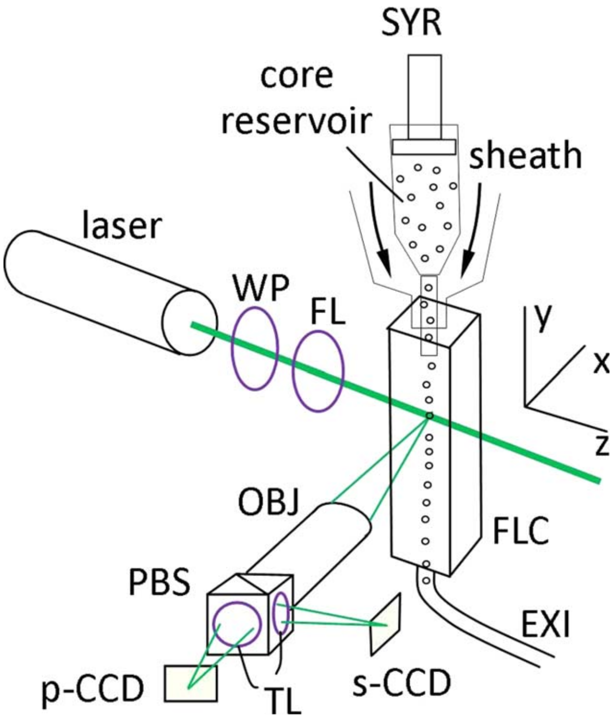

Figure 1. The schematic of a p-DIFC system: SYR, syringe; WP, half-wave plate; FL, focusing lens; FLC, flow chamber; EXI, exit tube; OBJ, objective; PBS, polarizing beam splitter; TL, tube lenses; CCD, camera recording either s- or p-polarized scattered light. [Color figure can be viewed in the online issue, which is available at wileyonlinelibrary.com.]

changed between cell measurements to reduce the number of saturated images during each measurement.

Diffraction Image Analysis and Cell Classification

After data acquisition, the image pairs with pixels of saturated intensities or of very weak total pixel intensities for both images were removed. Additional image pairs with large speckles were also removed since these have been shown to associate with cellular debris instead of intact cells (27). The diffraction images were then converted linearly from the 12-bit image format of the raw image data, denoted as I_{12}, into normalized image format of 8-bit pixel depth, I_8, in which the minimum and maximum pixel intensities in I_{12} were set to 0 and 255. The bit conversion is necessary to speed up the subsequent extraction of image parameters by the GLCM algorithm without significant loss of dynamic range (22,28). We have developed image processing software to extract 17 texture parameters from each normalized I_8 image based on the GLCM algorithm and 2 normalized parameters of minimum and maximum pixel intensities of the I_{12} image. The normalization of pixel intensities by the average pixel intensity was to remove the effect of different laser power used on different cell samples and beam polarization as noted in Table 1.

With the 19 parameters extracted from each image, the image processing software performs cell classification based on a supervised machine learning algorithm of support vector machine (SVM) using an open-source code package (libsvm 2.86) (29). Four types of kernel functions have been tested in this study: the Gaussian radial basis, sigmoid function, polynomial function, and linear function. A kernel function is employed in SVM to project each cell represented by its image parameters nonlinearly into a multidimensional space in which a hyperplane can be established to discriminate cells linearly with the largest margin (30).

The SVM based classification is executed in two steps: obtaining an optimized SVM model with a training set of data of known types and testing selected models in a test set of data of masked type identities. An SVM model consists of a specific combination of image parameters assembled into a feature vector and a kernel function that is used to map all imaged cells in a data set into a feature space for classification.

Table 1. Experimental parameters and classification results by the p-DIFC method

CELL SAMPLE SET	INCIDENT BEAM POLARIZATION	CELL TYPE	TOTAL IMAGE PAIR N_{TOT}	TRAINING IMAGE PAIR N_{TRA}	TEST IMAGE PAIR N_{TES}	MCC$_{\mathrm{av}}$[a]		A_{av}(%)[a]		FIRST 3 COMPONENTS OF FEATURE VECTOR[b] (N_c)
						TRAINING	TEST	TRAINING	TEST	
#1	Vertical	Jurkat	328	200	128	0.995	1.000	99.8	100	s-sa/s-m/s-nm (3)
		Ramos	253	200	53					
	Horizontal	Jurkat	1374	400	974	1.000	0.989	100	99.4	s-m/s-sa/s-se (4)
		Ramos	1046	400	646					
	45°	Jurkat	606	400	206	0.985	0.983	99.3	99.3	s-m/s-sa/se (7)
		Ramos	899	400	499					
#2	Vertical	Jurkat	1630	1000	630	0.966	0.950	98.3	97.8	Same as #1-vertical
		Ramos	1277	1000	277					
	Horizontal	Jurkat	1577	1000	577	0.957	0.960	97.9	98.1	Same as #1-horizontal
		Ramos	1885	1000	885					
	45°	Jurkat	899	700	199	0.628	0.578	81.4	83.8	Same as #1-45°
		Ramos	1530	700	830					

[a] The values of MCC$_{\mathrm{av}}$ and A_{av} were obtained with the optimized SVM model with N_c as the number of components in the feature vector and polynomial kernel function.

[b] GLCM and pixel intensity parameters: sa, sum average; m, mean; nm, normalized maximum pixel intensity; se, sum entropy (28); s, refers to the s-polarized diffraction image.

The dimensionality of the feature space of an SVM model is given by the number of components of or image parameters in its feature vector. A training process is to obtain an optimized SVM model with training data, which can be executed in two different approaches. One can fully evaluates all image parameters individually and rank them according to their classification accuracy. Then a sequence of feature vectors is constructed by adding the parameters one at a time according to their ranking with a selected kernel function for a set of SVM models. These models will be used to classify the imaged cells in a training data set and the one with highest accuracy is selected as the optimized one. Training SVM models in this approach is very computing intensive and took up to 10 days on five personal computers in the results presented here. SVM model training can be achieved in an expedited approach using an established SVM model by adjusting the numerical ranges of the parameters in its feature vector only, which takes at most a few hours to complete in comparison to the former approach with full training. In our study, we divided the image pairs in each data group of a specific beam polarization randomly into two data sets of training and test. The full training of SVM models was performed with the training data in the first cell sample in Table 1 to obtain an optimized SVM model. Then the same SVM model was trained expediently by the training data of the second cell sample.

In assessing the classification performance among different data sets, we define the following outcomes: TP as the number of correctly identified image pairs acquired from Ramos cells, TN as the number of correctly identified image pairs from Jurkat cells, FP as the number of image pairs of Jurkat cells but incorrectly identified as of Ramos cells, and FN as the number of image pairs of Ramos cells but incorrectly identified as of Jurkat cells. The total number of the image pairs in a data set is equal to the sum of TP, TN, FP, and FN. The classification accuracy A is defined as

$$A=\frac{\mathrm{TP}+\mathrm{TN}}{\mathrm{TP}+\mathrm{TN}+\mathrm{FP}+\mathrm{FN}}. \quad (1)$$

The Matthews correlation coefficient MCC is defined below as the other metric of classification performance

$$\mathrm{MCC}=\frac{\mathrm{TP}\times\mathrm{TN}-\mathrm{FP}\times\mathrm{FN}}{\sqrt{(\mathrm{TP}+\mathrm{FP})(\mathrm{TP}+\mathrm{FN})(\mathrm{TN}+\mathrm{FP})(\mathrm{TN}+\mathrm{FN})}}. \quad (2)$$

Different from the accuracy A, MCC accounts for both false-positive and false-negative errors with a value between 1 and −1 with 1 indicating a perfect classification and −1 a complete disagreement between the prediction and measurement.

Confocal Imaging and Reconstruction

The cells to be imaged were first double stained for nucleus and mitochondria with fluorescent dyes (Syto-61 and Mitotracker Orange, Life Technologies). A laser scanning confocal microscope (LSM 510, Zeiss) was used with a 63× water-immersion objective and a 4× scan zoom on the acquired image stacks. Each image stack consisted of about 40–60 slices with a 0.5 μm step size in air along the z-axis. The confocal image slices in a stack were first segmented using an in-house developed software followed by z-scale correction and interpolation of additional image slices for 3D reconstruction with cubic voxels (31). A total of 27 morphological parameters were calculated based on the voxels of the different cellular components in a reconstructed cell. We used the SPSS software (Version 19, IBM) to perform the two-sample *t*-tests of the 3D parameters and obtain respective *P*-values between the two cell lines.

RESULTS AND DISCUSSION

Measurement and Analysis of Diffraction Images by the p-DIFC Method

Two sets of samples were measured with the p-DIFC method on different days in which each set consisted of one Jurkat and one Ramos cell suspension sample. Cross-polarized diffraction image pairs of 12-bit pixels, I_{12}, were acquired from each of about 1,000–2,000 cells for each sample with linearly polarized incident beam varied among vertical, horizontal, and 45°. Figure 1 presents the experimental setup and Figure 2 shows examples of the normalized 8-bit image pairs, I_8, for each incident beam polarization. The GLCM based image processing yielded a total of 38 parameters from each image pair for an imaged cell and these parameters were assembled into feature vectors in different combinations to represent the imaged cells in a multidimensional feature space. We applied the SVM algorithm to statistically evaluate the feature vectors with the training data and obtain an optimized one for cell classification, which serves as the quantitative fingerprints for distinguishing the two cell lines. Table 1 lists the cell numbers in the training and test data sets of the two cell samples.

To obtain an optimized SVM model through full training, we first evaluated the individual performance of 38 image parameters based on A and MCC. Five tests of classification were conducted on the training data set for each parameter using an iterating scheme of five-fold cross-validation. The scheme randomly divides the training data set into five equal parts with one part being used as a test assembly and the remaining four parts as a training assembly. The procedure was repeated five times with A and MCC calculated each time to obtain their average values as A_{av} and MCCav. After ranking of the 38 image parameters with decreasing $\mathrm{MCC}_{\mathrm{av}}$, or A_{av} in the cases of divergent MCC, a total of 152 (=38 × 4) SVM models were established by adding the ranked image parameters one at a time to construct 38 feature vectors with each of the four kernel functions. Therefore, the feature vectors in a set of 38 SVM models with a selected kernel function have their number of components or image parameters increases from 1 to 38. Table 1 provides the definitions of top three image parameters and corresponding A_{av} and $\mathrm{MCC}_{\mathrm{av}}$ obtained with the polynomial kernel function in each training data set acquired with one of the three different beam polarizations

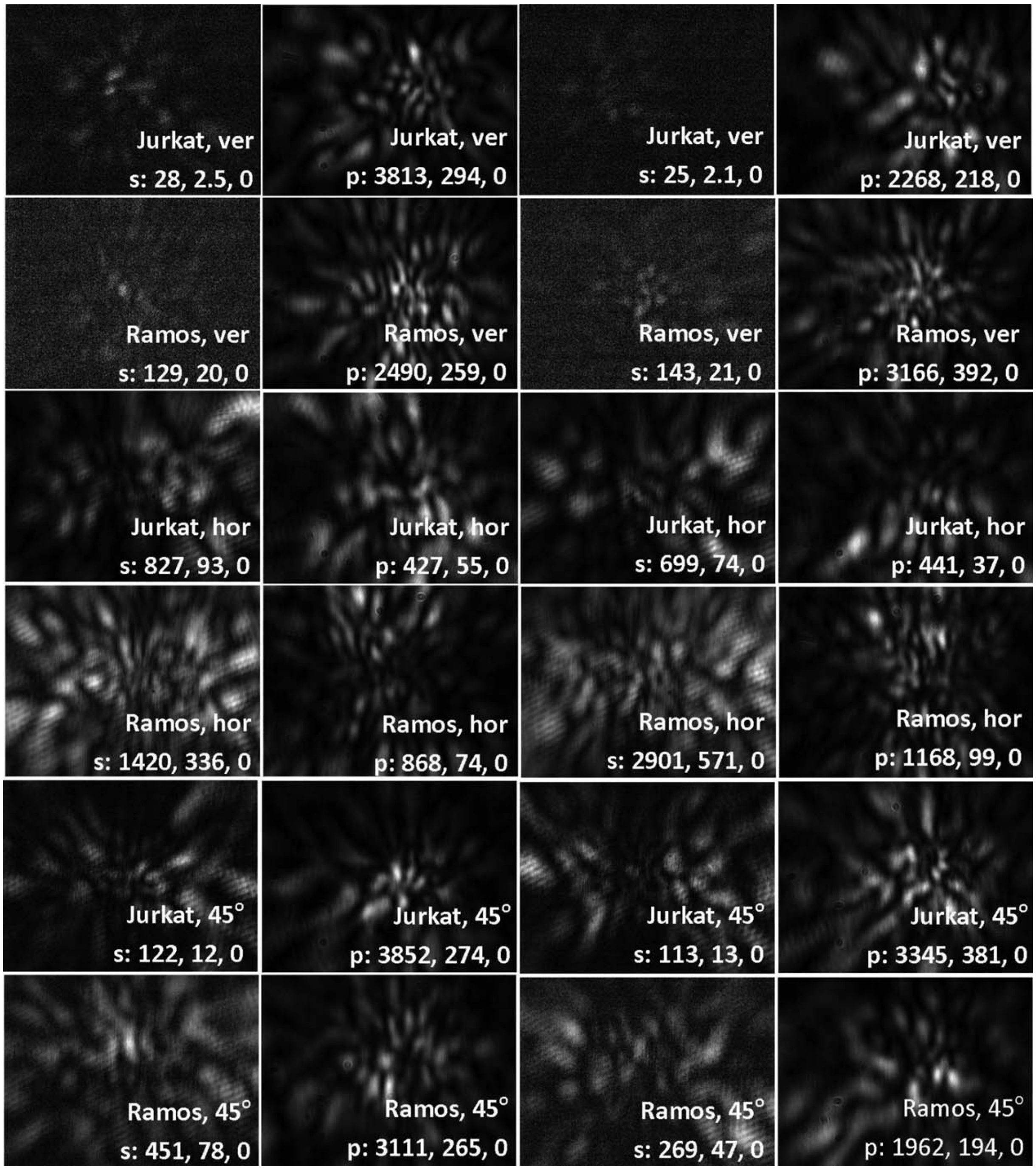

Figure 2. Examples of normalized cross-polarized image pairs of I_8 for two Jurkat and two Ramos cells in each group of beam polarization acquired from the first sample set. The white pixels are of maximum light intensity and black pixels of minimum intensity. Each image is labeled with the polarization of the incident beam, polarization of scattered light, maximum, average, and minimum pixel intensities of the corresponding I_{12} images.

for the first sample set. Figure 3 shows the performance of classification for four sets of SVM models with four different kernel functions in terms of A_{av} and MCC_{av} on the training data set. Additional data and classification results are provided in Table 1. One can see from Figure 3 that SVM models with both polynomial and linear kernel functions perform well for classification and the former does slightly better when applied to all data from both cell sample sets.

With these results we concluded that the accurate classification of the Jurkat and Ramos cells can be achieved robustly under the conditions of using either the polynomial or linear kernel function for the SVM model and the vertical or

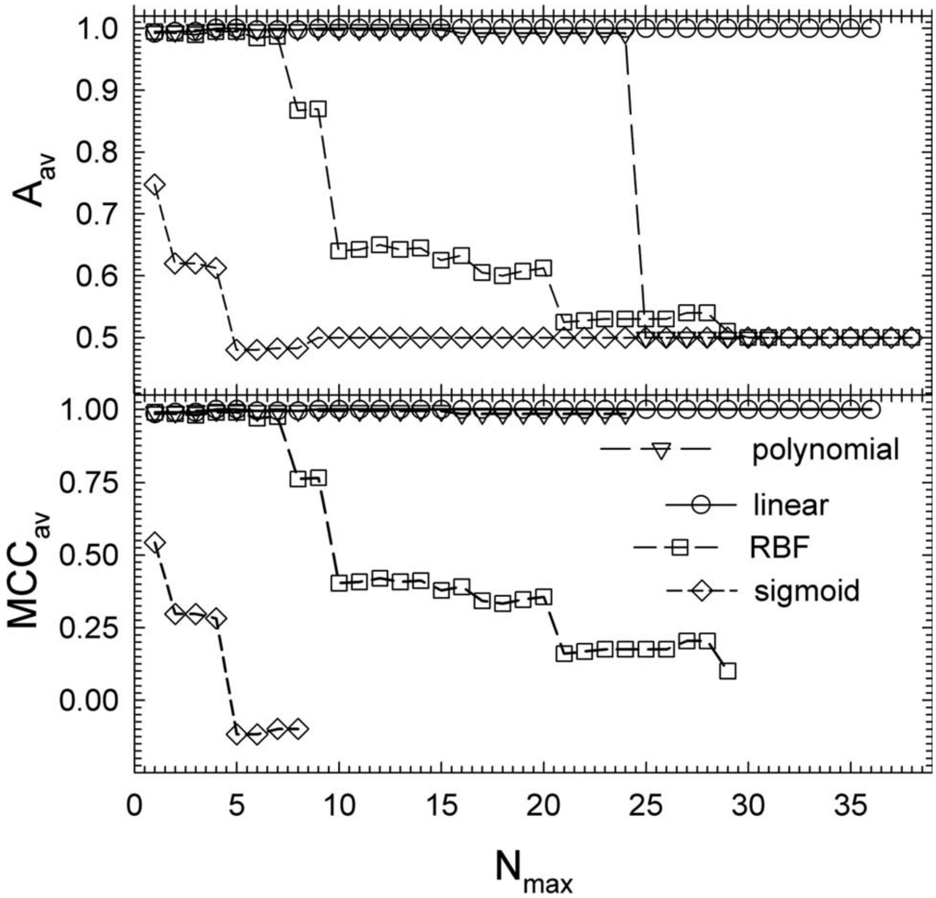

Figure 3. The averaged accuracy A_{av} and MCC_{av} versus the maximum number of image parameters in a feature vector N_{max}. The results were obtained by performing SVM classification with four different kernel functions in the training data set with feature vectors constructed by the image parameters sequenced according to their rankings. RBF denotes the Gaussian radial basis kernel function. The diffraction images were acquired from the first sample set with a vertically polarized incident laser beam. The lines are for visual guide.

horizontal for the incident beam polarization. The best overall results of A_{av} and MCC_{av} for classifying the Jurkat and Ramos cells were obtained with the polynomial kernel function and a feature vector of only three image parameters from the diffraction image pairs acquired with the vertical beam polarization.

Cell Measurement by the FCM Method

To acquire baseline data for comparison with the p-DIFC data, samples of the two cell lines were measured using a conventional FCM system (FACScan, Becton Dickinson). Cell samples were prepared under the condition of either unstained or co-stained by the anti-human T cell marker CD3 (CD0304, Life Technologies) and the B cell marker CD19 (MHCD1901, Life Technologies). Each sample measurement was performed on 10,000 cells. Light signals were acquired with a wavelength of 488 nm for excitation and scatter measurement, an emission filter centered at 578 nm for measurement of fluorescence by R-PE conjugated CD 3, and another filter centered at 519 nm for FITC conjugated CD19. Signal gating was implemented by the FSC and SSC signals to prevent the presence of debris, doublets, and triplets in the measured data. The plots of the light scatter signals presented in Figures 4A and 4B show clearly that the distributions of the angularly integrated light scatter signals of the two cell lines have significant overlap and they do not allow accurate classification of the two cell lines. The fluorescence signals in Figure 4C also confirm that the Jurkat cells are CD3+ and Ramos cells are CD19+ as expected.

Confocal Measurement and Quantitative Comparison of 3D Morphology

The Jurkat and Ramos cells were imaged with a confocal microscope followed by reconstruction for quantitative examination of their morphology using a previously in-house developed software (31) to understand the capability of the p-DIFC method for classifying the two cell lines. The 3D parameters were obtained from the reconstructed structures to compare their similarity and difference in morphology. Figure 5 represents perspective views of reconstructed cells of the two cell lines depicted in two colors with three major morphological parameters listed for each cell. By comparing these individual cells, one can clearly see that the morphology varies quite significantly even among the cells within the same line. A total

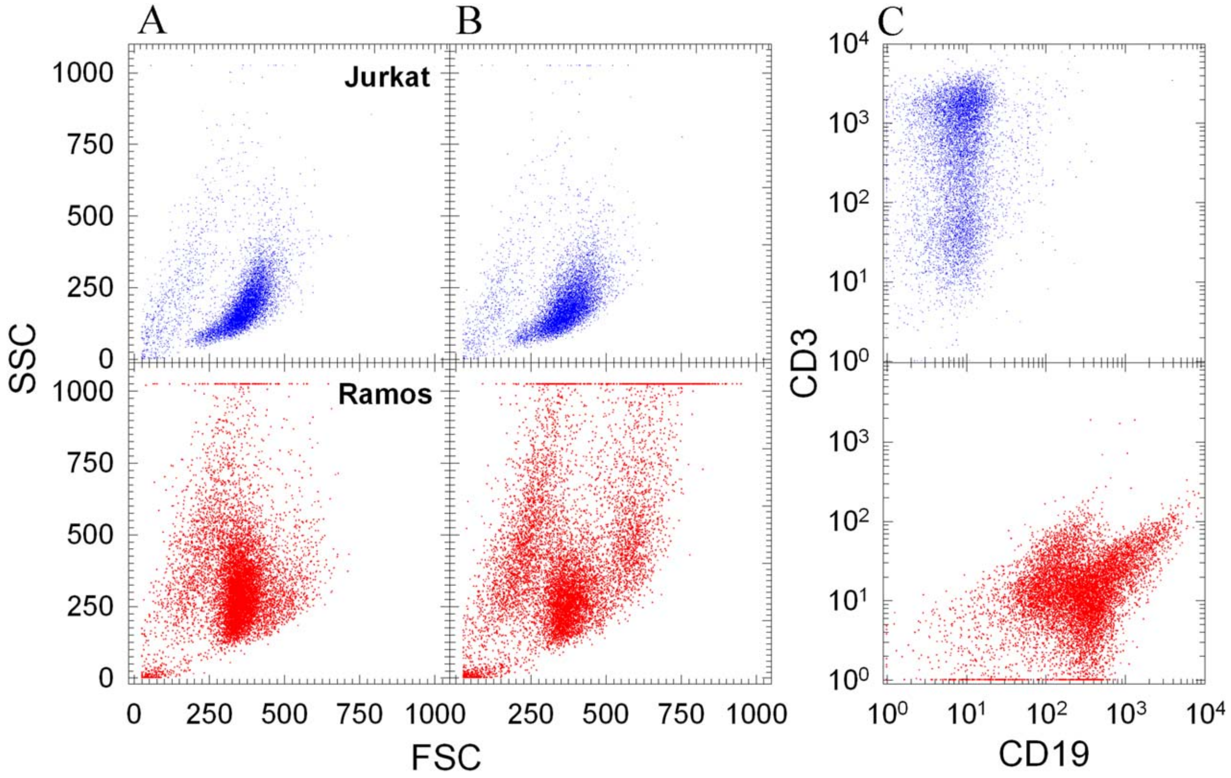

Figure 4. The scatter plots of the FCM data from 10,000 Jurkat or Ramos cells: (**A**) side (SSC) versus forward (FSC) light scatter signals of unstained cells with the mean values of the FSC(SSC) given by 352(193) and 341(332) for Jurkat and Ramos cells, respectively, and CV values by 24.7%(53.1%) and 27.5%(50.0%); (**B**) SSC versus FSC of cells co-stained by CD3 and CD19 with the mean values of the FSC(SSC) given by 355(189) and 375(414) for Jurkat and Ramos cells, respectively, and CV values by 24.3%(52.8%) and 27.5%(50.0%); (**C**) fluorescence signals of CD3 versus CD19 of the co-stained cells with the mean values of the CD19(CD3) given by 11.2(940) and 459(20.4) for Jurkat and Ramos cells, respectively, and CV values by 372%(102%) and 140%(192%). [Color figure can be viewed in the online issue, which is available at wileyonlinelibrary.com.]

of 45 Jurkat cells and 60 Ramos cells were imaged and analyzed, after which 27 parameters were obtained for individual cells to characterize their 3D morphology. Table 2 presents the values of mean and standard deviations of 16 key parameters derived from each of the two groups of 45 Jurkat and 60 Ramos cells. Table 2 also includes the results of statistical significance testing in terms of the *P*-value on the difference of parameters between the two cell groups. By examining the differences of the mean value, standard deviations and the *P*-value, one can confirm that the Jurkat and Ramos cells as two groups are highly similar in morphology in terms of their volumes, surface areas and shapes of the cell, nucleus and mitochondria. One exception is the volume ratios of nucleus to cell, which exhibits a statistically significant difference with $P < 0.05$. The parameters related to mitochondria exhibit considerable fluctuations as indicated by the relatively large standard deviations as a result of the small sizes of the organelles for imaging.

Comparison of the p-DIFC and 3D Morphology Data

The T and B subpopulations of lymphocytes were discovered by identifying their differences associated with immune responses (32,33) and the two cell types have been widely deemed as morphologically indistinguishable and can only be separated by fluorescent surface markers (34). Consequently accurate and label-free classification of the lymphocyte subpopulations or cell lines derived from them presents a challenge of fundamental interest (25) and is of practical importance to study of immune cells (35). Quantitative results of 3D morphological measurement show clearly that the two cell lines exhibit higher similarity between them than the case of the primary T and B cells extracted from human spleen tissues (data not shown here). Consequently the results reported present strong evidences in support of the p-DIFC method to extract and obtain an optimized set of diffraction image parameters as the "fingerprints" encoded by the 3D morphological traits of the imaged cells for classification.

We note from Table 1 that among the three polarization directions of the incident laser beam the vertical and horizontal polarizations yield the best results in distinguishing the Jurkat and Ramos cells. To understand the effect of beam polarization, a framework of Mueller–Jones matrices is useful (5,36). For the 45° polarized incident beam represented by a Jones vector, two 4×4 Mueller matrices can be used to express a cell's ability to scatter and the polarizing beam splitter to obtain the p-polarized scattered light as

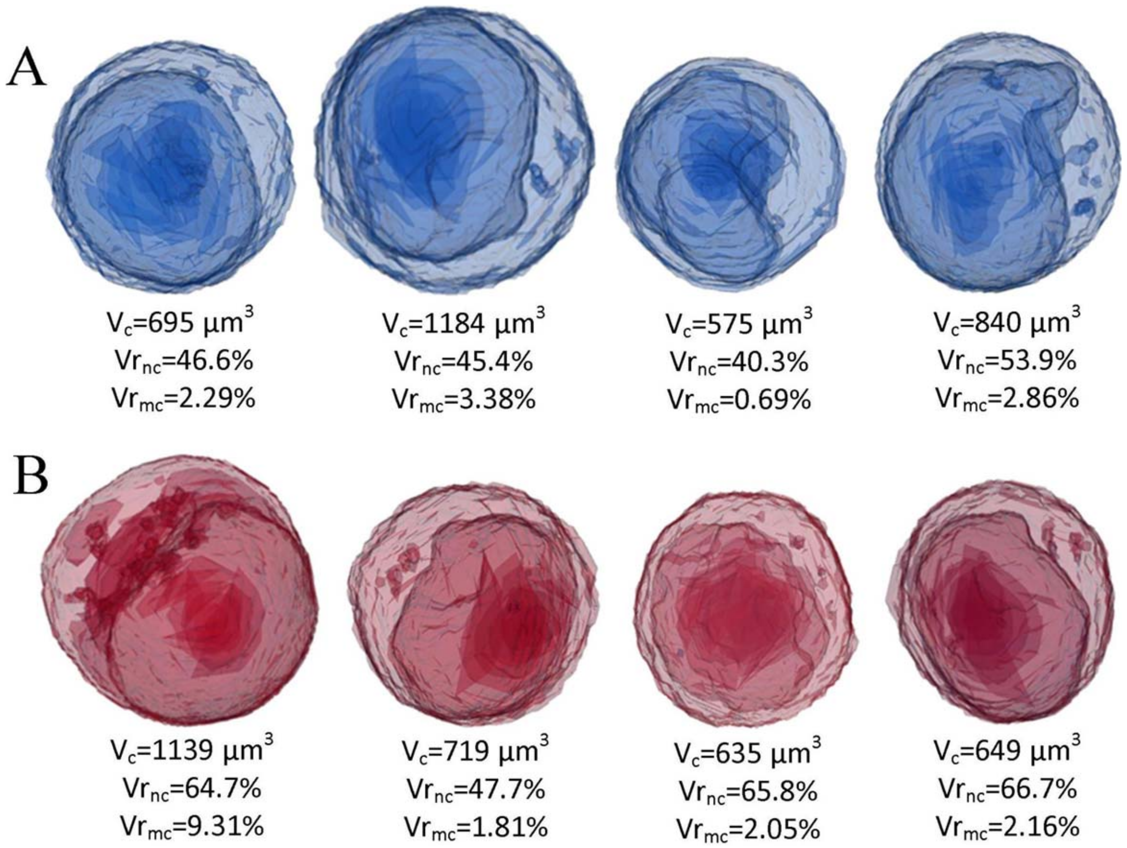

Figure 5. Perspective views of reconstructed 3D structures of individual (**A**) Jurkat and (**B**) Ramos cells (not to scale). The definitions of the morphological parameters are given in Table 2. [Color figure can be viewed in the online issue, which is available at wileyonlinelibrary.com.]

Table 2. Morphological parameters of Jurkat and Ramos cells

			MEAN ± STANDARD DEVIATION		
PARAMETER	SYMBOL	UNIT	JURKAT ($N = 45$)[a]	RAMOS ($N = 60$)[a]	P[a]
Cell volume	V_c[b]	μm^3	663.7 ± 308	666.5 ± 296	0.962
Cell surface area	S_c[c]	μm^2	36.85 ± 11.3	36.49 ± 10.7	0.867
Surface to volume ratio of cell	SVr_c	μm^{-1}	0.05954 ± 0.0121	0.05947 ± 0.0141	0.996
Index of surface irregularity of cell	ISI_c[d]	μm$^{-1/2}$	201.7 ± 28.5	199.7 ± 20.6	0.678
Average distance of cell membrane voxels to centroid	$<R_c>$	μm	6.797 ± 2.14	7.110 ± 2.45	0.495
Standard deviation of R_c	ΔR_c	μm	1.841 ± 0.721	2.051 ± 0.854	0.186
Nuclear volume	V_n	μm^3	407.8 ± 199	367.4 ± 185	0.285
Nuclear surface area	S_n	μm^2	29.79 ± 11.1	27.17 ± 9.09	0.187
Index of surface irregularity of nucleus	ISI_n	μm$^{-1/2}$	206.8 ± 42.1	204.3 ± 28.9	0.716
Mitochondrial volume	V_m	μm^3	33.40 ± 38.6	32.1 ± 34.8	0.853
Mitochondrial surface area	S_m	μm^2	40.48 ± 56.2	33.98 ± 51.0	0.538
Surface to volume ratio of mitochondria	SVr_m	μm^{-1}	0.9490 ± 0.266	0.8738 ± 0.199	0.100
Index of surface irregularity of mitochondria	ISI_m	μm$^{-1/2}$	731.3 ± 695	677.0 ± 550	0.656
Distance between the centroids of nucleus and cell	D_{nc}	μm	0.1760 ± 0.053	0.1597 ± 0.048	0.096
Volume ratio of nucleus to cell	Vr_{nc}	–	0.6280 ± 0.126	0.5479 ± 0.143	0.004
Volume ratio of mitochondrion to cell	Vr_{mc}	–	0.0526 ± 0.066	0.0484 ± 0.055	0.662

[a] n, number of imaged cells, P is based on a two-sample t-test method.
[b] $V = N_v \cdot V_0$ with N_v as the number of voxels inside the organelle of interest and V_0 as voxel volume.
[c] $S = N_s \cdot S_0$ with N_s as the number of voxels on the membrane of the organelle and S_0 as the side surface of voxel.
[d] $ISI = N_s \cdot a_0/(V)^{1/2}$ with a_0 as the side length (=0.07 μm) of voxel.

$$\begin{pmatrix} I_{\mathrm{p}} \\ Q_{\mathrm{p}} \\ U_{\mathrm{p}} \\ V_{\mathrm{p}} \end{pmatrix}_{45^\circ} = \begin{pmatrix} 1 & 1 & 0 & 0 \\ 1 & 1 & 0 & 0 \\ 0 & 0 & 0 & 0 \\ 0 & 0 & 0 & 0 \end{pmatrix} \begin{pmatrix} M_{11} & M_{12} & M_{13} & M_{14} \\ M_{21} & M_{22} & M_{23} & M_{24} \\ M_{31} & M_{32} & M_{33} & M_{34} \\ M_{41} & M_{42} & M_{43} & M_{44} \end{pmatrix} \begin{pmatrix} 1 \\ 0 \\ 1 \\ 0 \end{pmatrix} = \begin{pmatrix} M_{11}+M_{13}+M_{21}+M_{23} \\ M_{11}+M_{13}+M_{21}+M_{23} \\ M_{11}+M_{13}+M_{21}+M_{23} \\ M_{11}+M_{13}+M_{21}+M_{23} \end{pmatrix}. \tag{3}$$

It is easy to show that Eq. (3) leads to the pixel intensities of the p-polarized diffraction image recorded by a camera as angularly resolved distribution given below

$$I_{\mathrm{p},45^\circ} = (\mathrm{M}_{11}+\mathrm{M}_{13}) + (\mathrm{M}_{21}+\mathrm{M}_{23}). \tag{4}$$

Similarly, one can derive that the Jones vector for the s-polarized scattered light is given by

$$\begin{pmatrix} I_{\mathrm{s}} \\ Q_{\mathrm{s}} \\ U_{\mathrm{s}} \\ V_{\mathrm{s}} \end{pmatrix}_{45^\circ} = \begin{pmatrix} 1 & -1 & 0 & 0 \\ -1 & 1 & 0 & 0 \\ 0 & 0 & 0 & 0 \\ 0 & 0 & 0 & 0 \end{pmatrix} \begin{pmatrix} M_{11} & M_{12} & M_{13} & M_{14} \\ M_{21} & M_{22} & M_{23} & M_{24} \\ M_{31} & M_{32} & M_{33} & M_{34} \\ M_{41} & M_{42} & M_{43} & M_{44} \end{pmatrix} \begin{pmatrix} 1 \\ 0 \\ 1 \\ 0 \end{pmatrix} = \begin{pmatrix} M_{11}+M_{13}-M_{21}-M_{23} \\ -M_{11}-M_{13}+M_{21}+M_{23} \\ M_{11}+M_{13}+M_{21}+M_{23} \\ M_{11}+M_{13}+M_{21}+M_{23} \end{pmatrix}, \tag{5}$$

which yields the pixel intensities of the s-polarized images as

$$I_{\mathrm{s},45^\circ} = (M_{11}+M_{13}) - (M_{21}+M_{23}). \tag{6}$$

Using the same approach, we can show that the pixel intensities of each image pairs acquired with the incident beam of vertical and horizontal polarizations can be written as

$$I_{\mathrm{p,ver}} = (M_{11}-M_{12}) + (M_{21}-M_{22}), \tag{7}$$

$$I_{\mathrm{s,ver}} = (M_{11}-M_{12}) - (M_{21}-M_{22}), \tag{8}$$

and

$$I_{\mathrm{p,hor}} = (M_{11}+M_{12}) + (M_{21}+M_{22}), \tag{9}$$

$$I_{\mathrm{s,hor}} = (M_{11}+M_{12}) - (M_{21}+M_{22}). \tag{10}$$

By comparison of the above equations from Eq. (4) to (10), it becomes obvious that the different degrees of disparity between the p- and s-polarized diffraction images depends sensitively on certain elements M_{ij} of the imaged cell for different beam polarizations. If the vertical and horizontal beam polarization provides the maximum disparity, as indicated by the data in Table 1, then the elements M_{21} and M_{22} are most likely the responsible elements. These conclusions are supported by our previous measurements of the Mueller matrix elements of multiple HL-60 promyelocytic cells and NALM-6 pre-B cells using a goniometer, which show the high sensitivity of the elements M_{12}, M_{21}, M_{22}, and M_{23} to cell morphology (37).

The results yield strong evidences that the cross-polarized image pair acquired by the p-DIFC method adds an intriguing flow cytometric capability for cell classification. Specifically, the best result of classification was achieved for the incident beam of vertical polarization in Table 1 with three image parameters. Among the three, the first two are GLCM parameters of sum average and mean to quantify image texture (28) and the third one is a pixel intensity parameter of maximum-divided-by-mean, all calculated from the s-polarized images. Similarly, the best classfication for the incident beam of horizontal polarization was achieved with three GLCM parameters of sum average, sum entropy and mean together with the pixel intensity parameter of maximum-divided-by-mean from the s-polarized images. It is intersting to note that among the diffraction image pairs shown in Figure 2 the s-polarized images tend to have distinct textures than those in the p-polarized ones between the two cell lines. To quantitatively correlate these "fingerprints" image parameters to the morphological featus of cells, one needs to develop accurate models of light scattering by cellular structures as presented in Figure 5. We have previously established numerical methods (27,38), which are currently improved with detailed intracellular organelles such as mitochondria to obtain numerical and realistic polarized diffraction images through Eqs. (3) to (10) for clear understanding of the correlations between the GLCM parameters and morpohlogical features of the cells.

The mechanism underlying the p-DIFC ability to distinguish the two cell lines may be traced to the morphology of a cell in terms of its refractive index distribution. The two cell lines can be seen from the data in Table 2 to possess subtle but statistically significance differences in their nuclear and possibly mitochondria structures relative to the overall structures. While the differences are extremely difficult, if not impossible, to observe in two dimensional (2D) microscopic images, they nevertheless can quantified through 3D measurement. The possible correlation is consistent with the light scatter data between Figures 4A and 4B acquired from four different samples of 10,000 cells by the FCM system. Even though these signals are angularly integrated and do not allow accurate separation, a close examination produces clear evidences that the light scatter signals distribute quite differently between the two cell lines. Indeed, experimental and numerical modeling results of light scattering by biological cells by other researchers (39) as well as ours (6) support the conclusion that variations in nuclear morphology can produce quantifiable changes in the spatial distribution of unpolarized scattered light as represented by the element M_{11}. We have also analyzed numerically the effect of the nucleus and mitochondria on the patterns of diffraction images with previously developed finite-difference-time-domain (FDTD) and discrete-dipole-approximation (DDA) models of light scattering (22,27) using reconstructed 3D cell structures. The results suggest that the differences in nuclear volume, or the volume ratio of nucleus to cell as presented in Table 2, and shapes can lead to observable changes in the GLCM parameters extracted from the diffraction image data. The correlations of the changes between the nuclear morphology and GLCM parameters, however, are convoluted among the volume, shape and values of refractive index heterogeneity of the nucleus and mitochondria. Detailed numerical study is underway to understand their relations clearly and develop an effective mapping method.

CONCLUSION

We have shown through this study that the Jurkat T and Ramos B cells are of highly similar 3D morphology using a confocal imaging method. With the cross-polarized diffraction image pairs it has been demonstrated that the automated extraction of image texture and intensity parameters can serve as the "fingerprints" of a cell type, which enable robust and highly accurate classification of the two lymphocyte cell lines according to the subtle differences in nuclear morphology.

ACKNOWLEDGMENTS

We thank K. Dong for contribution to development of software for analysis of diffraction images and Y. Zhang for development of software for 3D reconstruction, M.K. McPeek and D.A. Weidner for helps on confocal microscopic and the conventional flow cytometric measurements of the cells.

LITERATURE CITED

1. Bickel WS, Davidson JF, Huffman DR, Kilkson R. Application of polarization effects in light scattering: A new biophysical tool. Proc Natl Acad Sci USA 1976;73:486–490.
2. de Grooth BG, Terstappen LW, Puppels GJ, Greve J. Light-scattering polarization measurements as a new parameter in flow cytometry. Cytometry 1987;8:539–544.
3. Dunn A, Smithpeter C, Welch AJ, Richards-Kortum R. Finite-difference time-domain simulation of light scattering from single cells. J Biomed Opt 1997;2:262–266.
4. Mourant JR, Johnson TM, Carpenter S, Guerra A, Aida T, Freyer JP. Polarized angular dependent spectroscopy of epithelial cells and epithelial cell nuclei to determine the size scale of scattering structures. J Biomed Opt 2002;7:378–387.
5. Lu JQ, Yang P, Hu XH. Simulations of light Scattering from a biconcave red blood cell using the FDTD method. J Biomed Opt 2005;10:024022.
6. Ding H, Lu JQ, Brock RS, McConnell TJ, Ojeda JF, Jacobs KM, Hu XH. Angle-resolved Mueller matrix study of light scattering by B-cells at three wavelengths of 442, 633 and 850 nm. J Biomed Opt 2007;12:034032.
7. Zhou X, Liu KY, Zhang N, Tan C. Simultaneous characterization of the shape and refractive index of transparent living cells by an optical aperture. Appl Opt 2010;49: 6416–6424.
8. Restifo NP, Dudley ME, Rosenberg SA. Adoptive immunotherapy for cancer: Harnessing the T cell response. Nat Rev Immunol 2012;12:269–281.
9. Aerts JG, Hegmans JP. Tumor-specific cytotoxic T cells are crucial for efficacy of immunomodulatory antibodies in patients with lung Cancer. Cancer Res 2013;73: 2381–2388.
10. Allard WJ, Matera J, Miller MC, Repollet M, Connelly MC, Rao C, Tibbe AG, Uhr JW, Terstappen LW. Tumor cells circulate in the peripheral blood of all major carcinomas but not in healthy subjects or patients with nonmalignant diseases. Clin Cancer Res 2004;10:6897–6904.
11. Chamberlain G, Fox J, Ashton B, Middleton J. Concise review: Mesenchymal stem cells: Their phenotype, differentiation capacity, immunological features, and potential for homing. Stem Cells 2007;25:2739–2749.
12. Hacker G. The morphology of apoptosis. Cell Tissue Res 2000;301:5–17.
13. Suratt BT, Young SK, Lieber J, Nick JA, Henson PM, Worthen GS. Neutrophil maturation and activation determine anatomic site of clearance from circulation. Am J Physiol Lung Cell Mol Physiol 2001;281:L913–L921.
14. Wyatt PJ. Identification of bacteria by differential light scattering. Nature 1969;221: 1257–1258.
15. Salzman GC, Crowell JM, Martin JC, Trujillo TT, Romero A, Mullaney PF, LaBauve PM. Cell classification by laser light scattering: Identification and separation of unstained leukocytes. Acta Cytol 1975;19:374–377.
16. Maltsev VP. Scanning flow cytometry for individual particle analysis. Rev Sci Instrum 2000;71:243–255.
17. Neukammer J, Gohlke C, Hope A, Wessel T, Rinneberg H. Angular distribution of light scattered by single biological cells and oriented particle agglomerates. Appl Opt 2003;42:6388–6397.
18. Singh K, Liu C, Capjack C, Rozmus W, Backhouse CJ. Analysis of cellular structure by light scattering measurements in a new cytometer design based on a liquid-core waveguide. IEE Proc Nanobiotechnol 2004;151:10–16.
19. Jacobs KM, Lu JQ, Hu XH. Development of a diffraction imaging flow cytometer. Opt Lett 2009;34:2985–2987.
20. Jacobs KM, Yang LV, Ding J, Ekpenyong AE, Castellone R, Lu JQ, Hu XH. Diffraction imaging of spheres and melanoma cells with a microscope objective. J Biophoton 2009;2:521–527.
21. Su X, Qiu Y, Marquez-Curtis L, Gupta M, Capjack CE, Rozmus W, Janowska-Wieczorek A, Tsui YY. Label-free and noninvasive optical detection of the distribution of nanometer-size mitochondria in single cells. J Biomed Opt 2011;16:067003.
22. Dong K, Feng Y, Jacobs KM, et al. Label-free classification of cultured cells through diffraction imaging. Biomed Opt Express 2011;2:1717–1726.
23. Sa Y, Zhang J, Moran MS, Lu JQ, Feng Y, Hu XH. A novel method of diffraction imaging flow cytometry for sizing microspheres. Opt Express 2012;20:22245–22251.
24. Zamai L, Falcieri E, Zauli G, Cataldi A, Vitale M. Optimal detection of apoptosis by flow cytometry depends on cell morphology. Cytometry 1993;14:891–897.
25. Strokotov DI, Yurkin MA, Gilev KV, van Bockstaele DR, Hoekstra AG, Rubtsov NB, Maltsev VP. Is there a difference between T- and B-lymphocyte morphology? J Biomed Opt 2009;14:064036–064012.
26. Sa Y, Feng Y, Jacobs KM, Yang J, Pan R, Gkigkitzis I, Lu JQ, Hu XH. Study of low speed flow cytometry for diffraction imaging with different chamber and nozzle designs. Cytometry A 2013;83A:1027–1033.
27. Zhang J, Feng Y, Moran MS, Lu JQ, Yang LV, Sa Y, Zhang N, Dong L, Hu XH. Analysis of cellular objects through diffraction images acquired by flow cytometry. Opt Express 2013;21:24819–24828.
28. Haralick RM. Statistical and structural approaches to texture. Proc IEEE 1979;67: 786–804.
29. Chang CC, Lin CJ. LIBSVM - A Library for Support Vector Machines. National Taiwan University; 2001.
30. Cortes C, Vapnik V. Support-vector networks. Mach Learn 1995;20:273–297.
31. Zhang Y, Feng Y, Justus CR, et al. Comparative study of 3D morphology and functions on genetically engineered mouse melanoma cells. Integr Biol 2012;4:1428–1436.
32. Raff MC. T and B lymphocytes and immune responses. Nature 1973;242:19–23.
33. LeBien TW, Tedder TF. B lymphocytes: How they develop and function. Blood 2008; 112:1570–1580.
34. Wintrobe MM, Lee GR. Wintrobe's Clinical Hematology, 10th ed, Vol. 1. Baltimore, MD: Williams & Wilkins; 1999. p 431.
35. Baitsch L, Fuertes-Marraco SA, Legat A, Meyer C, Speiser DE. The three main stumbling blocks for anticancer T cells. Trends Immunol 2012;33:364–372.
36. Bohren CF, Huffman DR. Absorption and Scattering of Light by Small Particles. New York: Wiley; 1983. p 65.
37. Ding H. Scattering of Light Waves by Biological Cells and in Tissues [Ph.D. Dissertation]. Greenville, NC: East Carolina University; 2006. 156 p.
38. Brock RS, Hu XH, Weidner DA, Mourant JR, Lu JQ. Effect of detailed cell structure on light scattering distribution: FDTD study of a B-cell with 3D structure constructed from confocal images. J Quant Spectrosc Radiat Transfer 2006;102:25–36.
39. Mourant JR, Canpolat M, Brocker C, Esponda-Ramos O, Johnson TM, Matanock A, Stetter K, Freyer JP. Light scattering from cells: The contribution of the nucleus and the effects of proliferative status. J Biomed Opt 2000;5:131–137.

CORRIGENDUM

Cytometry
PART A
Journal of the International Society for Advancement of Cytometry

ISAC
International Society for Advancement of Cytometry

Polarization Imaging and Classification of Jurkat T and Ramos B Cells Using a Flow Cytometer

Yuanming Feng, Ning Zhang, Kenneth M. Jacobs, Wenhuan Jiang, Li V. Yang, Zhigang Li, Jun Zhang, Jun Q. Lu, Xin-Hua Hu*

In the recently published Cytometry Part A article [85A: 817 – 826, 2014; doi: 10.1002/cyto.a.22504], the mean and standard deviation values of 5 parameters on the surface area and surface to volume ratio in Table 2 are erroneous due to a software mistake in area calculations. Other parameters including the *P*-values in Table 2 are correct and all discussion and conclusions remain unchanged. The corrected Table 2 should read as follows:

Table 2. Morphological parameters of Jurkat and Ramos cells

PARAMETER	SYMBOL	UNIT	MEAN ± STANDARD DEVIATION		P[a]
			JURKAT (N=45)[a]	RAMOS (N=60)[a]	
Cell volume	V_c[b]	μm^3	663.7 ± 308	666.5 ± 296	0.962
Cell surface area	S_c[c]	μm^2	526.4 ± 162	521.3 ± 153	0.867
Surface to volume ratio of cell	SVr_c	μm^{-1}	0.8495 ± 0.168	0.8493 ± 0.207	0.996
Index of surface irregularity of cell	ISI_c[d]	$\mu m^{-1/2}$	201.7 ± 28.5	199.7 ± 20.6	0.678
Average distance of cell membrane voxels to centroid	$<R_c>$	μm	6.797 ± 2.14	7.110 ± 2.45	0.495
Standard deviation of R_c	ΔR_c	μm	1.841 ± 0.721	2.051 ± 0.854	0.186
Nuclear volume	V_n	μm^3	407.8 ± 199	367.4 ± 185	0.285
Nuclear surface area	S_n	μm^2	425.5 ± 158	388.2 ± 130	0.187
Index of surface irregularity of nucleus	ISI_n	$\mu m^{-1/2}$	206.8 ± 42.1	204.3 ± 28.9	0.716
Mitochondrial volume	V_m	μm^3	33.40 ± 38.6	32.1 ± 34.8	0.853
Mitochondrial surface area	S_m	μm^2	578.3 ± 803	485.5 ± 728	0.538
Surface to volume ratio of mitochondria	SVr_m	μm^{-1}	13.56 ± 3.80	12.48 ± 2.84	0.100
Index of surface irregularity of mitochondria	ISI_m	$\mu m^{-1/2}$	731.3 ± 695	677.0 ± 550	0.656
Distance between the centroids of nucleus and cell	D_{nc}	μm	0.1760 ± 0.053	0.1597 ± 0.048	0.096
Volume ratio of nucleus to cell	Vr_{nc}	-	0.6280 ± 0.126	0.5479 ± 0.143	0.004
Volume ratio of mitochondrion to cell	Vr_{mc}	-	0.0526 ± 0.066	0.0484 ± 0.055	0.662

[a] n = number of imaged cells, *P* is based on a two-sample *t*-test method.
[b] $V = N_v \cdot V_0$ with N_v as the number of voxels inside the organelle of interest and V_0 as voxel volume.
[c] $S = N_s \cdot S_0$ with N_s as the number of voxels on the membrane of the organelle and S_0 as the side surface of voxel.
$ISI = N_s \cdot a_0/(V)^{1/2}$ with a_0 as the side length (=0.07μm) of voxel.

Received 20 March 2014; Accepted 18 July 2014

*Correspondence to: Xin-Hua Hu; Department of Biomedical Engineering, Tianjin University, Tianjin 300072, China. E-mail: hux@ecu.edu

DOI: 10.1002/cyto.a.22524